J. Electrochem. Sci. Eng. **12(4)** (2022) 685-701; http://dx.doi.org/10.5599/jese.1297

Open Access : : ISSN 1847-9286
www.jESE-online.org

Original scientific paper

Impact of the final thermal sealing of combined zinc/cerium oxide protective coating primers formed on low carbon steel

Stephan Kozhukharov[1,✉], Christian Girginov[2], Nelly Boshkova[3] and Alexandar Tzanev[4]

[1]*LAMAR Laboratory, University of Chemical Technology and Metallurgy, Sofia, Bulgaria*
[2]*Department of Physical Chemistry, University of Chemical Technology and Metallurgy, Sofia, Bulgaria*
[3]*Institute of Physical Chemistry – Bulgarian Academy of Science, Sofia, Bulgaria*
[4]*Institute of General and Inorganic Chemistry – Bulgarian Academy of Science, Sofia, Bulgaria*

Corresponding author: ✉s.kozhukharov@uctm.edu; Tel.: +359 899 837 282;

Received: February 13, 2022; Accepted: May 25, 2022; Published: June 13, 2022

Abstract

The final sealing possesses a proven beneficial effect on the protective properties of anodic oxide films on aluminum. In this sense, the present research is devoted to the evaluation of the impact of this procedure on the barrier ability of combined Zn/Ce oxide layers deposited on low carbon steel samples. For this purpose, four samples were submitted to galvanic zinc deposition, followed by spontaneous formation of cerium oxide primer layer (CeOPL). Afterwards, two of the samples underwent thermal sealing in boiling water in order to enhance their barrier ability. Its evaluation was performed by two electrochemical methods: electrochemical impedance spectroscopy (EIS) and potentiodynamic scanning (PDS) after 24 hours of exposure to a diluted model corrosive medium (MCM). Other instrumental methods were used in order to describe the effect of this final procedure on the color characteristics and hydrophobicity of the films. The results were collected from multiple tests, followed by statistical data treatment. In addition, the surfaces of the obtained films were submitted to direct observation by scanning electron microscopy (SEM), coupled with energy dispersion X-ray (EDX). Their composition was determined by means of X-ray Photoelectron Spectroscopy (XPS). The acquired data have revealed a detrimental effect of the final sealing in boiling water. It was expressed by the loss of the barrier properties of the Zn/CeOPL films, combined with additional decolorization and hydrophilization. Finally, the mechanism of this detrimental effect was determined by further SEM, EDX and XPS analyses.

Keywords

Zn-galvanization; cerium oxide primer layers (CeOPL); thermal sealing; barrier properties; surface analysis

Introduction

Unlike high-performance steels, the low-carbon ones are exceptionally susceptible to uniform corrosion even under moderate conditions. Furthermore, it is well known that the corrosion products of iron (*i.e.*, red rust) do not form dense layers, enabling continuous access of corrosive

species to the metallic surface beneath them. Hence, low-carbon steel corrodes until the complete destruction of the respective iron-based works/products. For this reason, the corrosion protection of these materials is indispensable.

On the one hand, galvanic zinc plating is a classical approach for processing low-carbon steel. It provides reliable corrosion protection of the steel substrates [1,2] and a suitable base for the deposition of other types of protective layers [3-5]. Besides, the optimization of the electrodeposition of Zn-based layers still remains a topic of intensive research [6,7]. In this sense, the main approaches for this optimization are through enhancement of the electrolyte composition [8-10] or by applying different electrodeposition regimes [11-13].

On the other hand, the successful formation of cerium conversion coatings on steel substrates was reported recently through both spontaneous [14-16] and electrochemical [17] deposition methods. Furthermore, this type of coatings is also proposed for further enhancement of zinc-phosphate finishing of steel [18]. Another recent trend is the formation of combined Ce/Ni [19] or Ce/V [20] conversion coatings on steel and magnesium alloys, revealing the versatility of this class of coatings and the possibilities to be combined with other elements and to be deposited on other metals and alloys.

Following these trends, the present brief research aims to assess and compare the basic physical characteristics of the obtained Zn/CeOPL double-layer coatings with and without additional thermal sealing in boiling water. Besides, the color-related features and wettability data were acquired after multiple measurements in order to be submitted to statistical data treatment. In addition, the mechanism of the impact of the final thermal treatment procedure was analyzed by detailed topological and compositional analyses.

Experimental

Electrochemical film deposition

The electrodeposition of the zinc coatings was performed on low-carbon steel plates (dimensions 30x30x1 mm) in a glass electrolytic cell with a volume of 300 ml. The applied current density was 2 A dm^{-2}, the pH was adjusted to 5 and the temperature was held in the range 20-25 °C. Metallurgical Zn was used for the anode. The electrolyte for the Zn film deposition was composed of two inorganic substances: $ZnSO_4.7H_2O$ (175 g dm^{-3}) and $(NH_4)_2SO_4$ (25 g dm^{-3}) with two organic additives: a mixture of polyethylene glycol and benzoic acid (40 g dm^{-3}) and benzalacetone, dissolved in ethanol (10 g dm^{-3}). This electrolyte was prepared following the optimal results reported in [21].

The further cerium oxide primer layers were formed by electroless deposition, again following the optimal compositions reported in previous works [22,23]. A mixture of $(NH_4)_2Ce(NO_3)_5$ and $CeCl_3$ (both with a concentration of 0.025 mol dm^{-3}) with the addition of 10 ml dm^{-3} 30 % H_2O_2 as deposition activator was used for the spontaneous formation of the cerium conversion coatings. The duration of this process was 15 min, at 50 ± 1 °C.

All the described procedures were performed on four samples, two of which were subjected to additional treatment in boiling distilled water for another 15 min. This approach has enabled to obtain two types of Zn/CeOPL coating primers: (i) two reference samples, without additional treatments, denoted as Ref_1 and Ref_2 and (ii) two thermally sealed specimens, marked as TS_1 and TS_2, respectively.

Electrochemical assessments

The electrochemical measurements were performed after 24-hour exposure to a 0.01 M NaCl solution, at room temperature, using a standard three-electrode flat corrosion test cell, according

to ISO 16773-2:2016, with a volume of 100 ml. This rather low concentration of NaCl in the model corrosive medium allows for distinguishing the differences among the acquired data from the respective samples. These assessments were performed by means of electrochemical impedance spectroscopy (EIS) and potentiodynamic scanning (PDS). The EIS spectra were acquired in 50 data points, distributed in the frequency range from 10 kHz to 0.01 Hz by applying an excitation signal of 10 mV, according to the open circuit potential (OCP). The respective OCP value was determined immediately prior to the acquisition of each spectrum.

The PDS curves were acquired in the potential range from -50 to +500 mV with respect to the reference electrode, with a potential sweep of 10 mV s^{-1}. This relatively high sweep rate allows for acquiring a rather wide range of PDS curves (total width of 550 mV) for quite a short time (55 s) of polarization.

These electrochemical measurements were performed with an Autolab PG-Stat30, equipped with a FRA2 frequency response analyzer (Metrohm, Netherlands). All measurements were performed against a Ag/AgCl/3M KCl reference electrodepositioned 10 mm above the horizontal corrosion test areas (1 cm^2). The electrochemical cells were completed with a cylindrical Pt-mesh, serving as a counter-electrode mounted around the reference electrode.

Color characteristics

The color characteristics of all samples were measured by operating a Lovibond RT100 tintometer. Three independent measurements were performed on different points on the surface of each sample. The objective was to determine the data repeatability acquired from one and the same sample surface in order to detect any color variation.

Contact angle measurements

The respective contact angles were measured using a “Theta Lite” high-precision optical device, a product of Biolin Scientific (UK), coupled with specialized “One attention” software (Finland). The constant volume of the drops was ensured using a “Gastight 1001” precise screw syringe, a product of Hamilton Co. (USA). The measurements were performed on three different points on the sample surfaces, similar to those in the previous section.

Statistical data treatment procedures

The electrochemical measurements were performed on two samples from each type. The EIS spectra were submitted to Kramers/Kroenig test (known as K/K test procedure), in order to determine the correspondence between the actual acquired EIS spectra from the samples and these of the used Model Equivalent Circuit (MEC). The test procedure is based on the presentation of each data point (n) of the corresponding EIS spectrum as a response of the respective RC circuit. The equivalent circuit for the execution of the K/K test is illustrated in Figure 1.

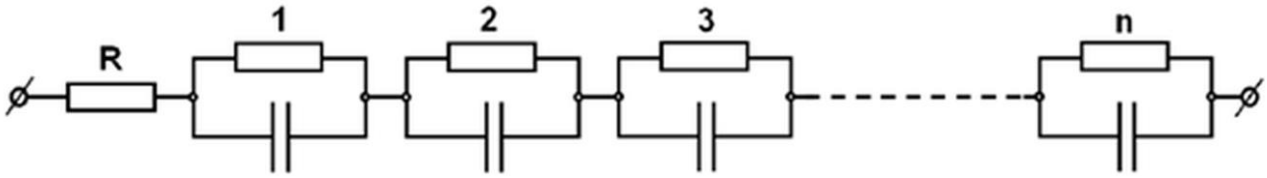

Figure 1. *Equivalent circuit for K/K test procedure, where in the present case n = 50 [24], R denotes the resistance of the electrolyte*

The acquired values from the K/K test procedure are listed in Table 1, together with the determined MEC component values.

The PDS curves were submitted to Tafel slope analyses. Next, the differences in the data acquired from every two samples were submitted to a simplified method, used in a previous work [25], based on Eq. (1):

$$AV = \frac{MV_2 + MV_1}{2} \pm \frac{MV_2 - MV_1}{2} \quad (1)$$

where AV is the average value; MV_2 is the higher measured value, whereas MV_1 is the lower measured value, respectively.

The data for characterization of the color characteristics and wettability of the investigated surfaces were acquired from three measurements for each sample. This approach allowed to obtain a total of 6 values for each parameter. The color characteristics were quantified according to CIE ($L^*a^*b^*$)-system, developed by International Commission on Illumination (abbreviated CIE) in 1976 [26]. There, the parameter L^* (luminosity) varies from 0 to 100 and accounts for the color brightness. The other vector parameters, a* and b*, vary from -128 to 127, showing the transition from yellow to blue and red to green, respectively. The acquired values of these color parameters were submitted to statistical data treatment, performed in 7 consecutive steps, described in the algorithm used in [27] and illustrated in Figure 2.

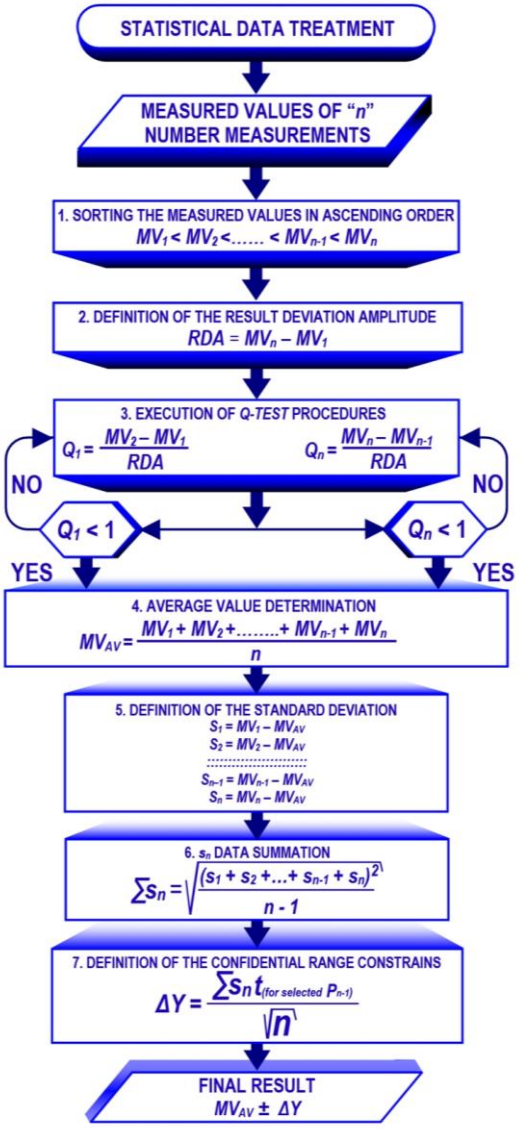

Figure 2. *Algorithm for statistical data treatment*

This algorithm was applied for six measurements (n = 6) for each group (*i.e.,* three measurements on two samples) and the value of the Student criterion was selected to be t = 5.959 [24], at probability P = 0.1 %.

The obtained values for the contact angles were also submitted to this statistical analysis in order to determine the impact of the thermal treatment on the surface properties of the Zn/CeOPL films, as well as their uniformity (from the respective standard deviations).

Topological and compositional analysis of the surface

This analysis was performed by means of three instrumental methods: (i) scanning electron microscopy (Tescan, SEM/FIB Lyra I XMU), (ii) energy dispersive X-Ray map analysis (Quantax 200 X-ray spectrometer, Brueker) and (iii) X-ray photoelectron spectroscopy (VG Escalab II). The latter uses AlKα radiation with an energy of 1486.6 eV, with a chamber pressure of 1.33×10^{-7} Pa. The C1s line of adventitious carbon at 284.6 eV was used as an internal standard to calibrate the binding energies. The photoelectron spectra were corrected by subtracting a Shirley-type background and were quantified using the peak area and Scofield's photo-ionization cross-section. The accuracy of the binding energy (*BE*) measurements was ± 0.2 eV.

Results and discussion

Electrochemical assessment

The EIS spectra, shown in Figure 3, undoubtedly reveal the detrimental effect of the treatment of the already deposited Zn/CeOPL films in boiling water. Indeed, the Bode plots show that the $|Z|$ / (f) dependence acquired for the reference samples lies above the thermally treated ones. The same trend is observable for the -phase shift / (f) diagrams. It does not reach -90°, revealing that the electric double layers formed between the sample surfaces and the liquid MCM are strongly irregular and do not form perfect capacitance. The phase shift of the reference samples is almost twice as higher (reaching about 60°) as this of the thermally treated (at around 30°).

Consequently, the final treatment by boiling water leads to deterioration of the obtained Zn/CeOPL films. The deterioration of the Zn/CeOPL layer is even more obvious when comparing the respective Nyquist plots. There, the semi-circles of the reference samples are quite larger than those of the thermally treated ones. Indeed, the value of the real part Z' of Ref_1 and Ref_2 reaches 45 and 35 kΩ cm^2, whereas the semi-circles of TS_1 and TS_2 do not reach even 10 kΩ cm^2.

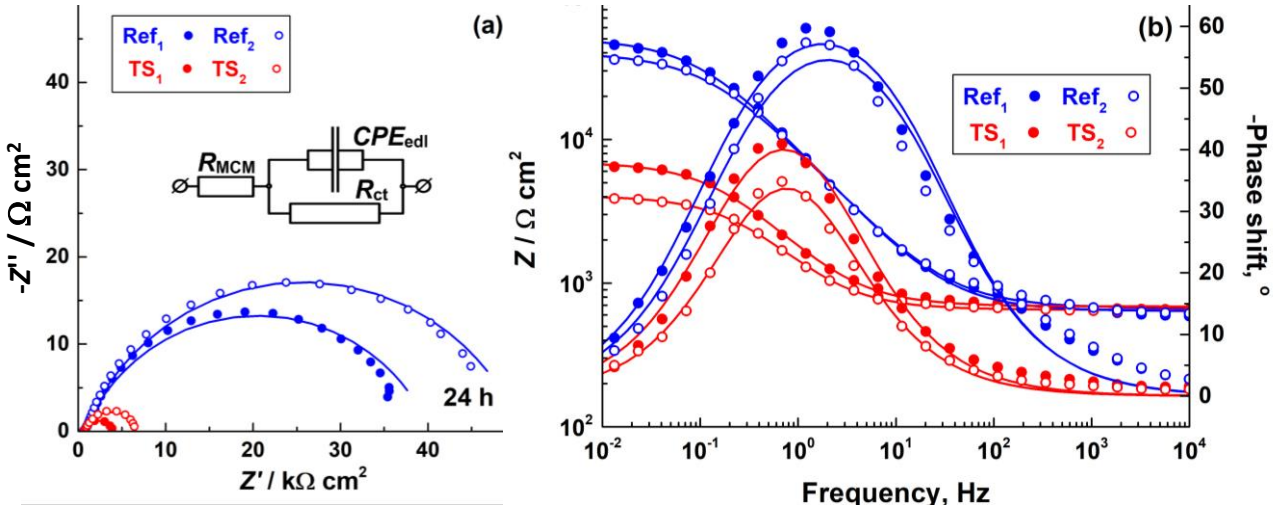

Figure 3. *EIS spectra in Nyquist (a) and Bode (b) plots of the investigated samples (symbols denote experimental data, while lines - the respective fitted spectra)*

The spectra, shown in Figure 3, were submitted to further analysis by means of fitting to a suitable Model Equivalent Circuit (MEC). It was composed of three elements, which correspond to the resistance of the model corrosive medium (R_{MCM}), the constant phase element of the interface between the sample surface and the medium (CPE_{edl}) and the charge transfer resistance (R_{ct}). This MEC consists of a simple Randles cell, which perfectly reveals the actual behavior of conducting layers exposed to an electrolyte [28]. The acquired numerical data are summarized in Table 1.

Table 1. *Numerical data acquired by fitting of the obtained EIS spectra to the MEC, illustrated in the inset of Figure 3*

Sample	R_{MCM} / Ω cm^2	CPE_{edl} / s^n Ω^{-1} cm^{-2} 10^{-6}	n	R_{ct} / kΩ cm^2
Ref_1	636.00 ± 10.78	28.13 ± 0.78	0.76 ± 0.01	50.10 ± 1.51
Ref_2	670.00 ± 14.70	29.17 ± 1.07	0.75 ± 0.01	39.60 ± 1.41
TS_1	687.00 ± 6.44	159.30 ± 4.05	0.78 ± 0.01	6.30 ± 0.13
TS_2	687.00 ± 6.44	214.40 ± 4.37	0.78 ± 0.01	3.41 ± 0.05

The values of R_{MCM} are noticeably similar for all samples. Their somewhat high values are a consequence of the relatively low NaCl concentration of the MCM. The constant phase element of the electric double layer (CPE_{edl}) is by an entire order of magnitude higher for the samples submitted to final thermal sealing in boiling water. This fact reveals deterioration of the capacitive reactance caused by the thermal treatment. Consequently, the boiling water causes partial leaching of the cerium oxides/hydroxides formed on the surface of the Zn/CeOPL coating. This suggestion is confirmed by the R_{ct} values, which for the thermally treated specimens are also lower by an entire order of magnitude than those of the reference samples. Hence, the average R_{ct} value for the reference samples is about 44.85 kΩ cm^2, whereas, for the thermally sealed ones, it reaches 4.86 kΩ cm^2. The lower R_{ct} values, in this case, are an indication of the loss of insulating properties of the Ce-oxides and hydroxides, which compose the CeOPL layer, probably due to its partial leaching.

Each EIS spectrum acquisition was followed by performing a potentiodynamic scan (PDS), the obtained curves are presented in Figure 4.

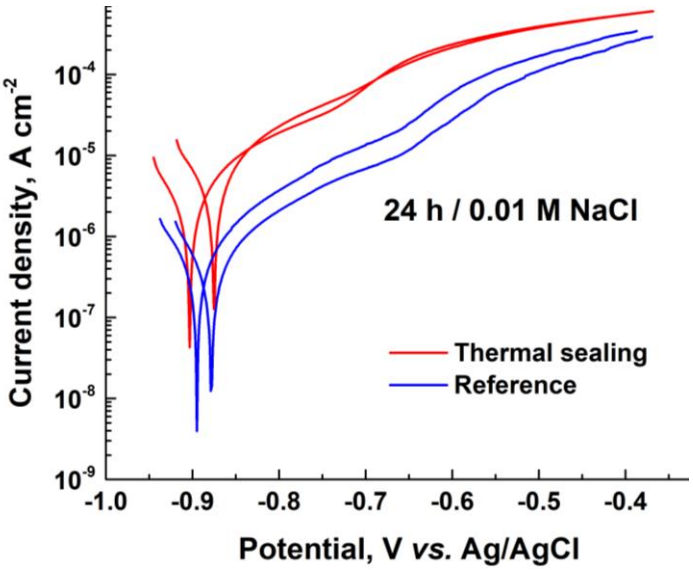

Figure 4. *PDS curves acquired from the investigated specimens after 24 hours of exposure to 0.01 M NaCl model corrosive medium*

Figure 4 shows that the PDS curves of the reference samples lie below those of the samples, treated in boiling water. Besides, an overlapping of the anodic branches is observed for the reference samples, unlike the thermally sealed ones. This fact reveals that probably the treatment for

15 minutes in boiling water results in the partial removal of Ce-compounds from the Zn/CeOPL films. These inferences are confirmed by the results of the Tafel slope analysis, summarized in Table 2.

Table 2. *Numerical results acquired from the Tafel slope analysis of the PDS curves recorded after 24 hours of exposure to the model corrosive medium*

Parameter	Sample			
	Ref_1	Ref_2	TS_1	TS_2
Polarization resistance, kΩ cm^2	49.18	39.09	6.31	3.67
Average value	44.16 ± 5.05		4.99 ± 1.32	
Corrosion potential, mV	-878	-895	-903	-932
Average value	-886.50 ± 8.50		-917.50 ± 14.50	

Indeed, the data in Table 2 show that the analysis of respective PDS curves confirms the results of the EIS spectra. The values of the polarization resistance of the investigated samples are almost equal to the charge transfer resistance ($R_p \approx R_{ct}$). The average values of the corrosion potential, calculated from Eq. 1, are close to -900 mV. The simultaneous appearance of distinguishable R_p values for the respective sample groups and the relatively similar corrosion potentials was the reason for determining the effect of the final thermal sealing on other physical properties of the obtained Zn/CeOPL films.

Color characteristics and wettability

The color parameters presented in Table 3 reveal that the Zn/CeOPL coatings do not suffer any drastic changes in brightness (L^*) and in the red/green vector (a^*).

Only weak brightening (from L^*_{av} = 75.95 ± 0.01 of the references to L^*_{av} = 78.56 ± 0.01 for the thermally treated samples) was observed as a result of the probable partial detachment of the yellow cerium oxide/hydroxide deposits provoked by the formation of water vapor bubbles in the boiling water. As a result, uncovered white areas of the electrodeposited Zn layer appear, resulting in the observed brightening.

Table 3. *Color characteristics of the investigated surfaces*

Sample	Measurement number	***L****	**a***	**b***
Ref_1	1	76.72	-0.33	54.86
	2	76.86	-1.61	54.10
	3	75.32	-0.29	53.65
Ref_2	1	74.20	-2.39	55.77
	2	76.26	-2.54	52.09
	3	76.33	-1.57	52.78
	Average value	75.95 ± 0.01	-1.455 ± 0.006	53.875 ± 0.006
TS_1	1	75.23	-6.03	-2.48
	2	80.73	-7.39	-2.00
	3	75.88	-6.45	-1.54
TS_2	1	79.05	-7.25	-5.08
	2	83.62	-6.93	-0.21
	3	76.86	-5.67	-0.28
	Average value	78.56 ± 0.01	-6.62 ± 0.01	-1.92 ± 0.09

The values of a^* tend to zero for both types of samples. This means that there are no traces of red-rust, despite the definitely acidic properties of the Ce-containing deposition solutions evinced in previous works [29] and confirmed by other authors [30]. The insignificant transition of the red/green color vector (from a^*_{avg} = -1.455 ± 0.006 for the references to a^*_{avg} = -6.62 ± 0.01 for the

thermally treated ones) is most probably due to the appearance of spots of $FeOH_2$ caused by the boiling water, as this compound is green in color.

However, a sharp decay of the values of the yellow/blue vector (from b^*_{avg} = 53.875 ± 0.006 to about b^*_{avg} = -1.92 ± 0.09) shows a transition from yellow to gray. Indeed, the gold-like look described by other authors, as well [31,32], has disappeared due to the thermal treatment. Similar observations have been reported with respect to the post-treatment of a cerium conversion coating on AA2024-T3 by boiling in dilute $NH_4H_2PO_4$ solution [33].

Since the Zn/CeOPL films are intended for initial layers of multilayered coating systems, such as the proposed in [34,35], their surface properties are of key importance for the adhesion of the subsequent intermediate and finishing layers. In this sense, systematic measurements of the contact angle were performed in order to define whether the elaborated Zn/CeOPL films are more suitable for hydrophilic or for hydrophobic coating layers. This additional analysis is rather important in order to avoid potential blistering or delamination across the Zn/CeOPL coating primer and the further organic, inorganic, or hybrid coating layers.

Figure 5 represents the results of the systematic drop tests performed on the investigated samples. The images clearly show that the reference samples (Ref_1 and Ref_2) possess relatively hydrophobic properties, whereas the thermally treated ones (TS_1 and TS_2) are hydrophilic.

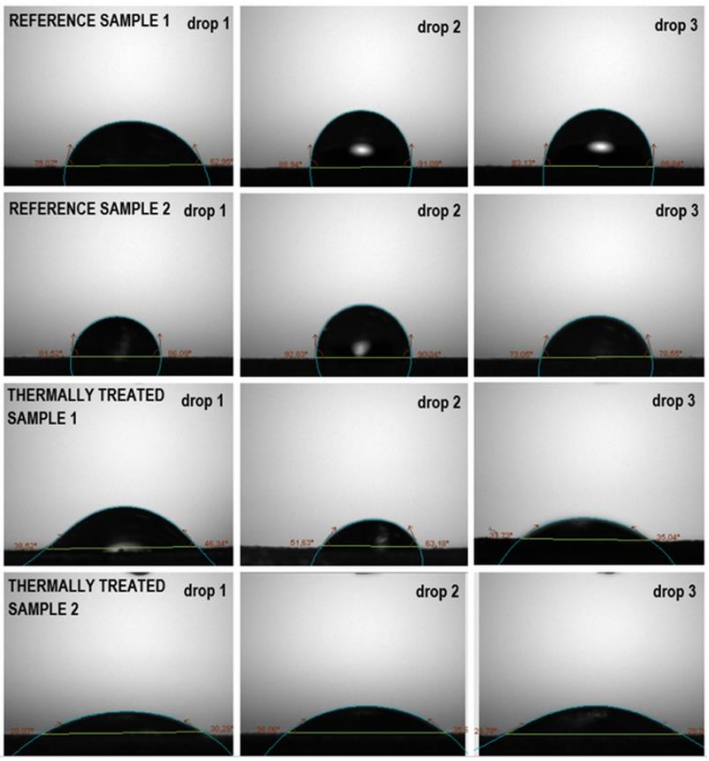

Figure 5. *Profiles of the interfaces between the surfaces of the investigated samples and distilled water drops after 10 s of contact*

The obtained results, shown in Figure 5, were further submitted to statistical analysis, following the seven-step procedure illustrated in Figure 2. The results show that the reference samples possess almost hydrophobic properties, with the average wetting angle θ_{avg} tending to 90°, whereas the value of θ_{avg} of the thermally sealed ones is below 40°. All results, including the raw data (the measured values) and these from the statistical treatment, are presented in Table 4.

The surprising detrimental effect of the final thermal treatment has imposed the need to analyze the cause of its occurrence. In this sense, it was of interest to determine the deterioration mechanism by performing additional topological and compositional analyses, which are interpreted in the next paragraph.

Table 4. *Data on the wetting angle of the investigated samples*

Sample	Measurement number	Left angle, °	Right angle, °
Ref_1	1	75.07	62.95
	2	88.94	91.09
	3	83.13	88.84
Ref_2	1	81.52	86.09
	2	92.83	90.34
	3	73.05	78.55
	Average value	$\Theta_{avg} = (82.70 \pm 0.01)$ °	
TS_1	1	38.52	46.34
	2	51.79	63.26
	3	37.73	35.04
TS_2	1	28.07	30.28
	2	36.05	35.64
	3	25.78	28.28
	Average value	$\Theta_{avg} = (38.07 \pm 0.01)$ °	

Surface topological and compositional analysis

This analysis was performed by scanning electron microscopy (SEM) combined with energy dispersion X-ray (EDX) spectroscopy.

Both the SEM images and the EDX maps reveal that the uniform Zn/CeOPL films undergo cracking due to the submission to the final sealing procedure, as shown in Figure 6.

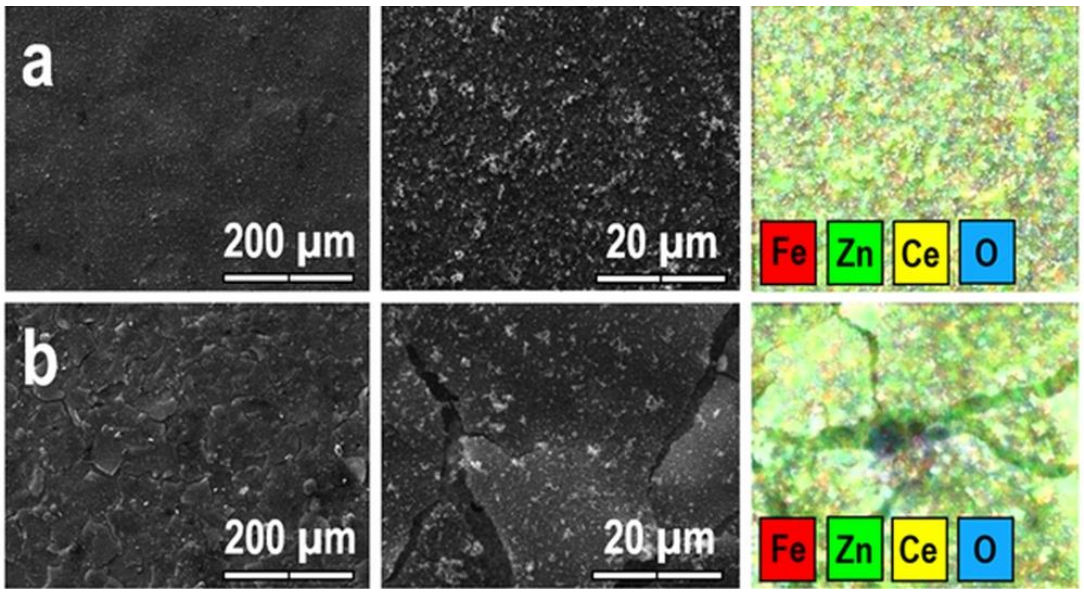

Figure 6. *Low- and high-resolution SEM images and EDX maps of Zn/CeOPL coating primer before (a) and after (b) the additional sealing*

There are several possible reasons that could cause the cracking of the Zn/CeOPL films during the final sealing in boiling water. For instance, the difference in the thermal expansion coefficients of the steel substrate, the primary Zn layer and the Ce-oxide/hydroxide coating result in tension stress across the interfaces between the layers. These stresses appear at the beginning of the thermal sealing, as well as after this process when the sample undergoes re-cooling. During these stages, the temperature of the sample changes in the range between 20 and 100 °C. In addition, the cracks that have already appeared expand due to water uptake and also due to the formation of water vapor inside them. Hence, the already penetrated water forms vapor bubbles, exfoliating parts of the Zn/CeOPL layer.

The additional cross-sectional SEM images in Figure 7 reveal that the film deterioration proceeds mainly at the interface between the Cerium oxide/hydroxide layer and the galvanic Zn sublayer.

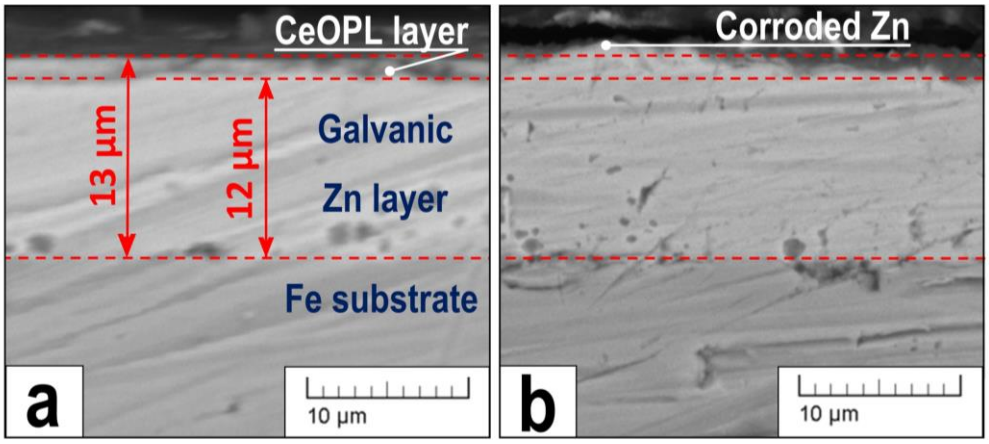

Figure 7. *Cross-sectional SEM images of Zn/CeOPL layers before (a) and after (b) the thermal sealing*

As it can be seen from the figure, the electroplated Zn layer is much thicker (being about 12 µm) than the CeOPL upper layer (approximately 1 µm). Consequently, the difference between the thicknesses of these layers is an additional reason for the preferential deterioration exactly at the interface between these layers. Besides, as a rule of thumb, metals like the Fe substrate and the Zn galvanic layer possess rather higher thermal expansion coefficients compared to the Ce-oxide/hydroxide upper layer, since its composition resembles this of CeO_2 based glasses and ceramics. Further, comparing positions (a) and (b) of Figure 7, it becomes clear that in the former case, the coating is composed of two distinguishable layers, whereas in the latter case, the thermal sealing causes obvious deterioration.

Another probable reason is the change in the chemical composition of the layer due to the hydration of both Ce-oxides and metallic Zn underneath. This results in swelling of the film and further increase of mechanical stresses in its structure.

Both phenomena, film cracking and hydration, result in changes in the physical properties described in the previous sections. Indeed, the cracks facilitate water uptake of the thermally treated (TS_1 and TS_2) layers, making them more hydrophilic compared to the reference samples (Ref_1 and Ref_2). Of course, this effect is further enhanced by the hydrated surface obtained during the final sealing. Besides, the loss of yellow tonality results from the partial leaching of the Ce-oxide/hydroxides from the Zn/CeOPL films because of water penetration and bubble formation during the film treatment in boiling water.

The potential impact of these probable film deterioration factors was further analyzed by X-ray photoelectron spectroscopy. Specimens of both types were submitted to XPS analysis in order to elucidate the deterioration mechanism caused by the final thermal treatment procedure. The elemental compositions of the reference and thermally treated samples in atomic percentages are presented in Table 5.

Table 5. *Element composition of Zn/CeOPL coating primers before and after the final thermal sealing established by XPS*

	Content, at.%				Content, %*	
Sample	C	O	Zn	Ce (total)	Ce^{3+}	Ce^{4+}
Reference	45.1	37.4	3.5	14.0	11.5	88.5
Thermally sealed	30.9	48.0	17.9	3.2	23.8	76.2

*Both contents are calculated as a part of the total Ce-content

The data in Table 5 undoubtedly reveal that the thermal sealing causes depletion of Ce with simultaneous Zn enrichment. Indeed, the concentration of cerium decreases by more than four times, while the concentration of Zn increases by almost 6 times. Both phenomena reveal the separation of CeOPL proposed in the previous paragraph, which reveals areas of the surface of the galvanic Zn layer. Based on the data in this table, it could be inferred that 12.3 at.% of Ce(IV) oxides and hydroxides undergo a reduction with respect to Ce(III) compounds. This result is acquired by calculation of the integrated peak area at 916.7 eV, following the equation of Pardo et al. [36]. This peak for both samples is illustrated in Figure 8a (third peak marked as Ce^{4+} at 916.7 eV). Ce3d core photoelectron spectra in Figure 8a are characterized by a complex structure due to the hybridization of the cerium ions with the ligands of oxygen orbitals and partial occupation of the 4f valence orbital. As a result, a spin-orbital splitting appears in the doublet peaks, whereupon each doublet has an additional structure, owing to the effect of the final state [37]. The decrease in the intensities of the Ce peaks confirms the decrease in the total Ce content.

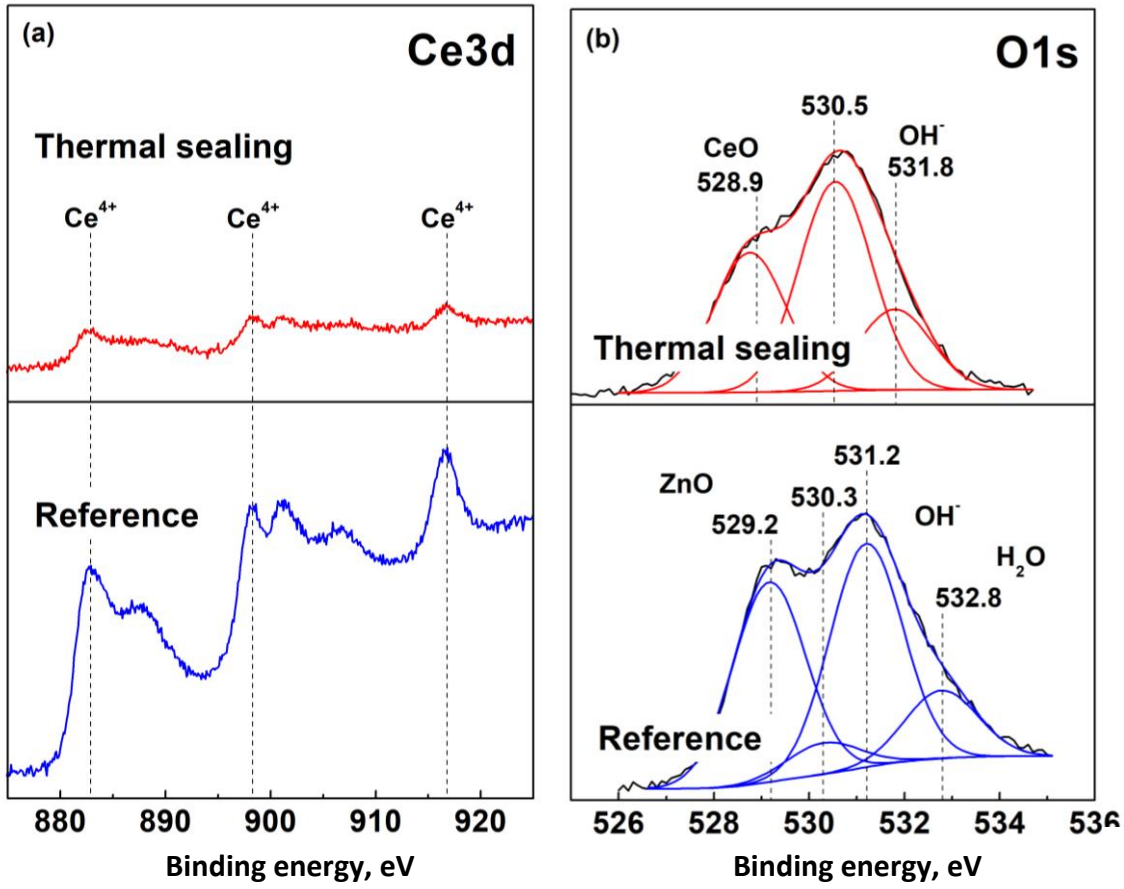

Figure 8. *Ce3d characteristic peaks for ceria (a) and deconvolution of the characteristic peaks of O1s (b)*

Figure 8b shows the deconvolution performed on the O1s spectra of both types of samples. The O1s core electron spectrum of the reference sample is divided into four peaks. The first peak, situated at 529.2 eV is characteristic of the presence of oxygen ions bonded with Ce [38]. The second one, at 530.3 eV, could be ascribed to the occurrence of oxygen atoms coordinated with Zn atoms in the ZnO lattice [39]. The third (at 531.2 eV) and fourth (at 532.8 eV) peaks in Figure 8b are related to the presence of hydroxide ions and both physically adsorbed and crystal hydrate water [40], respectively.

In the case of the thermally sealed coating primer, the occurrence of chemically bonded oxygen (Ce-O and Zn-O) appears. The peaks for ZnO (at 530.5 eV) are much more intensive with respect to those of the reference sample. At the same time, the Ce-O peak (528.9 eV) decreases after the thermal sealing. Hence, obviously, parts of the CeOPL upper layer undergo detachment, uncovering areas

covered by the inner galvanic Zn layer. The quantity of the OH^--groups at 531.8 eV also decreases, as a result of the thermal treatment. Surprisingly, the peak characteristic for adsorbed water disappears. This is possible due to the high temperature of the sample during its withdrawal from the boiling water and its cooling to room temperature is accompanied by intensive water evaporation.

The Zn2p core photoelectron spectra are shown in Figure 9a. The Zn2p peak is positioned at 1021.4 eV, and its spin-orbital splitting is 23.1 eV. In the case of the thermally treated samples, a weak shift of the Zn2p peaks appears towards higher binding energies. Here, the value of the calculated modified Auger parameter is 2010.0 eV for the reference sample, compared to 2010.3 eV, calculated for the thermally treated specimen. Following Al-Gaashani *et al.* [41], it could be inferred that these characteristic peaks reveal the conversion of the Zn-galvanic layer to ZnO during the formation of Zn/CeOPL.

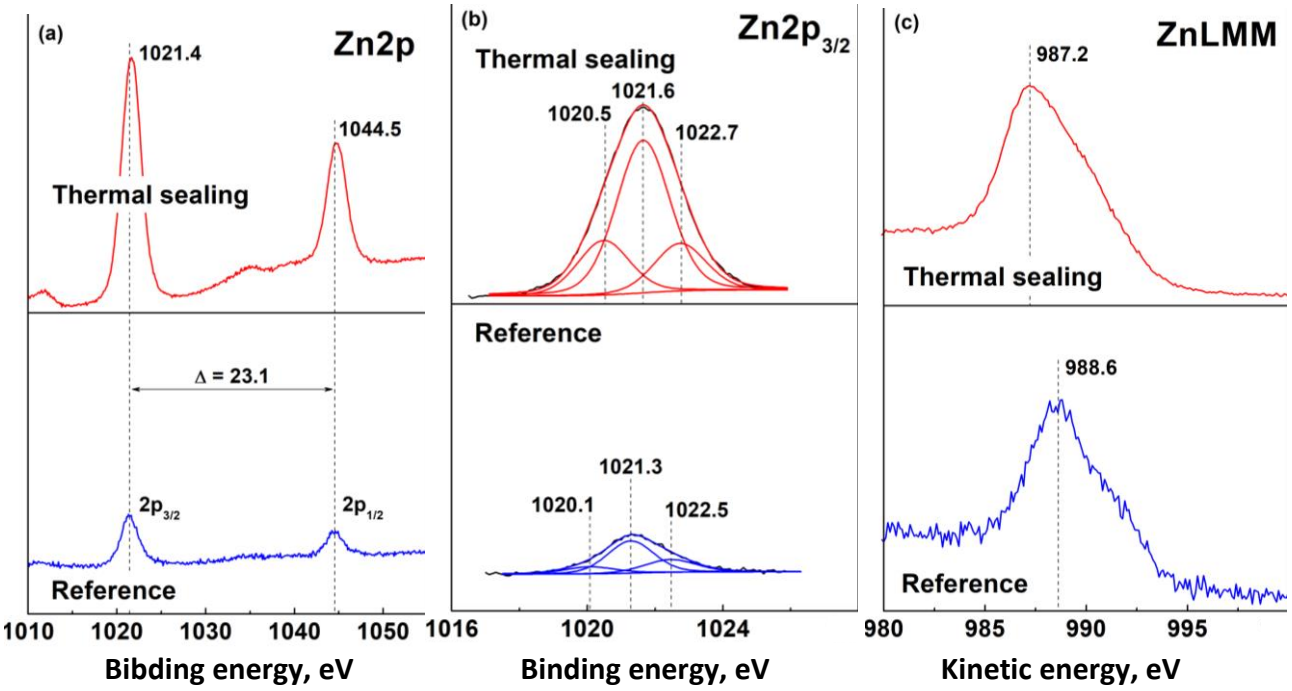

Figure 9. *Zn2p core electron spectra of the reference and the thermally sealed samples (a), deconvolution of the characteristic peaks for Zn2p (b) and Auger ZnLMM spectra (c)*

The peaks of $Zn2p_{3/2}$ spectra in Figure 9b are relatively wide and asymmetric, showing the coexistence of various Zn-compounds. For this reason, the $Zn2p_{3/2}$ spectrum presented in Fig 9b was deconvoluted, which led to the detection of three individual peaks at 1020.1 - 1020.5 eV, 1021.3 - 1021.6 eV and 1022.5 - 1022.7 eV, respectively. The low binding energy of the first peak shows weak bonds between Zn ions and other positively charged particles, such as Ce^{4+}/Ce^{3+} or carbon [42], whereas the other two peaks are typical for ZnO and $Zn(OH)_2$. The percentage ratios of these peaks to the total Zn-content for the reference sample are as follows: 15 % for the peak at 1020.1 eV, 59 % for the one at 1021.3 eV and 26 % for the third at 1022.5 eV. For the thermally treated sample, these percentages are 21, 61 and 18 %, respectively. Consequently, some quantities of metallic Zn in the Zn/CeOPL layer undergo oxidation during the thermal treatment. This conclusion is further confirmed by the pattern of the Auger peaks (Figure 9b).

The comparison of the C1s spectra for the reference and the thermally sealed samples in Figure 10 reveals the appearance of an additional peak at 283.5 eV. This peak suggests the appearance of carbide compounds [43,44] due to the additional thermal treatment. The other three peaks,

positioned at 284.5 eV, 285.3 - 285.8 eV and 285.5 eV are characteristic of the occurrence of a variety of (C–C), (C–OH) or (C–O–C) bonded carbons and even (C=O) bonds [45].

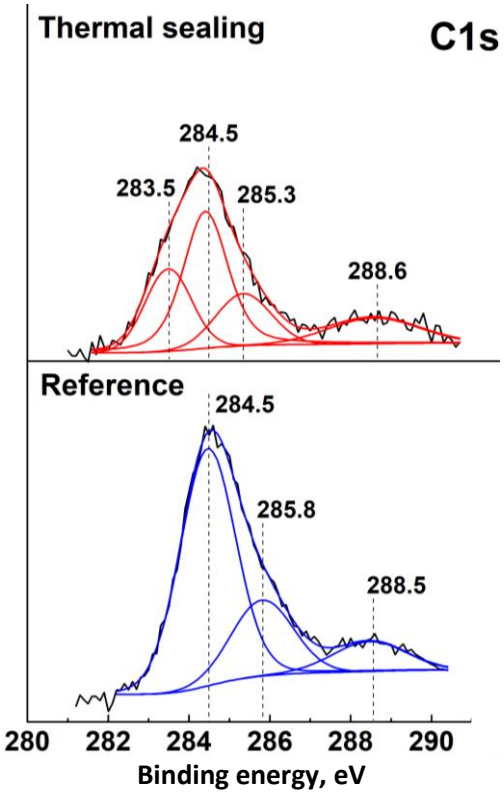

Figure 10. *C1s spectra of the investigated samples*

The occurrence of a considerable amount of carbon originates from the used organic additives described in the experimental part.

Finally, no Fe2p spectrum was detected even at passing energy of 50 (*i.e.*, with a more sensitive analysis). This fact indicates that the inner Zn layer continues to efficiently protect the low carbon steel, even after the partial destruction of the upper CeOPL layer during the thermal treatment. After collecting all assessment data, a conceptual model was created, illustrated in Figure 11.

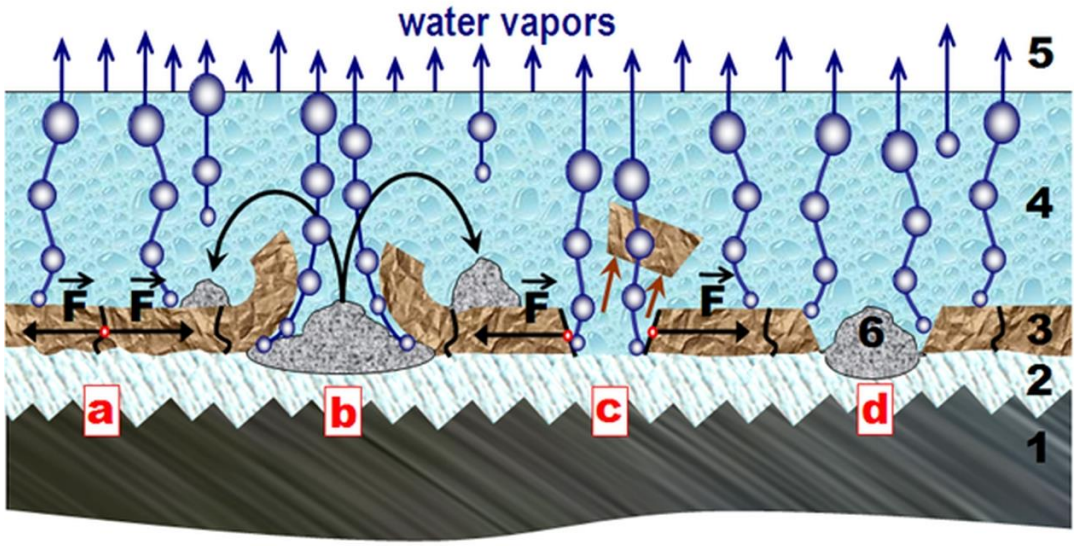

Figure 11. *Schematic illustration of the deterioration processes caused by the thermal treatment of the Zn/CeOPL coating primer: 1) low carbon steel substrate; 2) inner galvanic Zn layer; 3) CeOPL outer layer; 4) boiling water; 5) ambient air and 6) corrosion products of the Zn-galvanic layer*

The immersing of the Zn/CeOPL coated samples into boiling water causes tensile stresses (indicated with the letter *F* in Figure 11) due to the dilatation of the metallic substrate and the galvanic layer. These stresses appear as a consequence of the difference in the thermal expansion coefficients of the respective layers (Figure 11a). Probably, the reduction of Ce(IV) oxides and hydroxides to the respective Ce(III) compounds also contributes to the CeOPL cracking, causing defects in its structure. Afterwards, the entrapment of boiling water through the resulting ruptures in the CeOPL leads to partial dissolution of the organic compounds (see the experimental section) and localized corrosion on the surface of the Zn layer. Besides, water vapor bubbles appear on the boundaries between the galvanic Zn layer and the subsequent CeOPL. The growing vapor bubbles and the expansion of the ZnO and $Zn(OH)_2$ corrosion products result in further enhancement of the mechanical stress inside the CeOPL cracks. As a result, these ruptures convert to centers of CeOPL delamination (Figure 11b). Similar undercoating wedge effects, which favor corrosion, are observed and explained in detail by other authors [46-48], as well. Besides, re-deposition of Zn-corrosion products occurs on the intact areas surrounding the delaminated areas. This re-deposition is favored by the outward hydrodynamic fluxes promoted by the boiling water bubbles.

Coincidently, direct detachment of CeOPL fragments is also possible among the adjacent cracks, again enhanced by the bubbling of the boiling water (Figure 11c) inside these cracks. Finally, the areas of the Zn layer, uncovered by the CeOPL detachment, become centers of Zn-corrosion (Figure 11d). Here, it should be appointed that the Zn oxidation (corrosion) could be further enhanced by the reduction of Ce(IV) compounds to Ce(III) ones. It should also be noted that the present conceptual model excludes any direct CeOPL dissolution effects due to the extremely low solubility of the Ce(III)/Ce(IV) oxides and hydroxides, established by Aramaky [49] and confirmed by the model, proposed by Scholes *et al.* [50].

After the withdrawal of the thermally treated samples from the boiling water, the high temperature results in intensive evaporation of water from their surface. This accelerated drying probably has an additional contribution to the resulting Zn/CeOPL deterioration.

Finally, the proposed conceptual model completely explains the changes in the contents of all the elements shown in Table 5.

Conclusions

Systematic comparative research of the impact of the final thermal sealing is performed on Zn/CeOPL coating primers deposited on low carbon steel substrates. These combined coating primers were formed by deposition of galvanic Zn film, followed by the formation of cerium oxide primer layer (CeOPL).

The results from the electrochemical tests performed by means of EIS and PDS in a dilute model corrosive medium have shown obvious deterioration of the barrier ability of the thermally sealed layers. The detrimental effect of this final procedure was registered by the sharp change of the EIS spectra and confirmed by their further analysis using a suitable model equivalent circuit. Furthermore, the potentiodynamic curves have revealed a sharp drop in the polarization resistance by an entire order of magnitude due to the thermal sealing.

The comparative statistical analysis of the data acquired for the physical properties (color characteristics and wettability) of the investigated samples has shown an obvious loss of the gold-like look and hydrophobicity of the Zn/CeOPL films after the thermal sealing.

The topological and compositional analyses (via SEM and EDX) have undoubtedly revealed the appearance of cracks and ruptures in the Zn/CeOPL films, combined with partial exfoliation of the formed Ce-oxides and hydroxides.

The research activities were completed by detailed XPS analysis in order to describe the alteration of the contents of all elements composing the combined Zn/CeOPL coating primer. The results have shown depletion of the Ce content, accompanied by partial reduction of Ce(IV) to Ce(III) compounds. An increase in Zn content was registered due to uncovering of areas of the galvanic Zn layer caused by CeOPL cracking, delamination and detachment. These phenomena are followed by partial superficial Zn corrosion. No traces of Fe were found, evincing that the Zn-Ce-O deterioration proceeds on the interface between the Zn galvanic layer and the finishing CeOPL.

The combination of all used analytical methods has enabled to determine the mechanism of the detrimental effect of the final sealing on the barrier properties and the physical characteristics of the obtained Zn-Ce-O coating primers. It was established that severe cracking appears due to mechanical tensions in the film structure and is combined with an alteration of its chemical composition.

Summarizing all the obtained results, a brief conceptual model was created and even illustrated for explication of all the Zn-Ce-O coating primer deterioration processes. It reveals that the interface between the galvanic Zn layer and the spontaneously deposited CeOPL is rather susceptible to Zn-Ce-O coating deterioration. Consequently, additional treatments of the already formed Zn layers are necessary prior to the subsequent CeOPL deposition.

Acknowledgements: *The financial support of the Bulgarian National Scientific Fund under contract No. КП-06-Н37/16 "New environmentally friendly one- and multi-layer coatings for corrosion protection of structural materials with wide application" is gratefully acknowledged. Also, equipment supplied by INFRAMAT (contract No. D01-382/2020 with Bulgarian Ministry of Education and Science) is used in the present investigations.*

References

[1] A. El Fazazi, M. Ouakki, M. Cherkaoui, *Journal of Bio- and Tribo-Corrosion* **7** (2021) 58. https://doi.org/10.1007/s40735-021-00482-y

[2] G. Zhao, W. Zhang M. Zhao, *International Journal of Electrochemical Science* **17** (2022) 220134. https://doi.org/10.20964/2022.01.38

[3] N. Boshkova, N. Tabakova, G. Atanassova, N. Boshkov, *Coatings* **9** (2019) 487. https://doi.org/10.3390/coatings9080487

[4] M. Chotirach, P. Rattanawaleedirojn, Y. Boonyongmaneerat, R. Chanajaree, K. Schmid, M. Metzner, N. Rodthongkum, *Materials Chemistry and Physics* **277** (2022) 125567. https://doi.org/10.1016/j.matchemphys.2021.125567

[5] F. Gao, J. Mu, Z. Bi, S. Wang, Z. Li, *Progress in Organic Coatings* **151** (2021) 106071. https://doi.org/10.1016/j.porgcoat.2020.106071

[6] E. A. Alvarenga, J. G. Moreira, V. T. L. Buono, V. F. C. Lins, *Materials and Corrosion* **61** (2010) 421-427. https://doi.org/10.1002/maco.200905360

[7] A. Medjaldi, A. Himour, M. Bououdina, S. Ouchenane, A. Gharbi, *Metallography, Microstructure and Analysis* **10** (2021) 208-218. https://doi.org/10.1007/s13632-021-00728-8

[8] P. S. Basak, *IOSR Journal of Applied Chemistry* **14** (2021) 10-15. https://doi.org/10.9790/5736-1409011015

[9] K. Jyotheender, M. Kumar, C. Srivastava, *Surface and Coatings Technology* **423** (2021) 127594. https://doi.org/10.1016/j.surfcoat.2021.127594

[10] K. Jyotheender, C. Srivastava, *Microscopy and Microanalysis* **27** (2021) 2498-2499. https://doi.org/10.1017/S1431927621008916
[11] M. Ohba, T. Scarazzato, D. C. R. Espinosa, Z. Panossian, *Electrochimica Acta* **309** (2019) 86-103. https://doi.org/10.1016/j.electacta.2019.04.074
[12] L. Fuller, J. Martin, Y. Ma, S. King, S. Sen, *Chemistry Select* **6** (2021) 5426-5434. https://doi.org/10.1002/slct.202101193
[13] S. Kireev, A. Yangurazova, S. Kireeva, *IOP Conference Series Materials Science and Engineering* **862** (2020) 062024. https://doi.org/10.1088/1757-899X/862/6/062024
[14] J. Xu, S. S. Xin, P. H. Han, R. Y. Ma, M. C. Li, *Materials and Corrosion* **64** (2013) 619-624. https://doi.org/10.1002/maco.201206752
[15] C. Wang, F. Jiang, F. Wang, *Corrosion Science* **46** (2004) 75-89. https://doi.org/10.1016/S0010-938X(03)00135-5
[16] M. R. Majdi, I. Danaee, S. S. Afghahi, *Materials Research* **20** (2017) 445-451. https://doi.org/10.1590/1980-5373-MR-2016-0661
[17] J. Creus, F. Brezault, C. Rebere, M. Gadouleau, *Surface and Coatings Technology* **200** (2006) 4636-4645. https://doi.org/10.1016/j.surfcoat.2005.04.027
[18] B. Ramezanzadeh, H. Vakili, R. Amini, *Journal of Industrial and Engineering Chemistry* **30** (2015) 225-233. https://doi.org/10.1016/j.jiec.2015.05.026
[19] H. Hasannejad, T. Shahrabi, M. Jafarian, *Materials and Corrosion* **64** (2013) 1104-1113. https://doi.org/10.1002/maco.201106484
[20] X. Jiang, R. Guo, S. Jiang, *Journal of Magnesium and Alloys* **4** (2016) 230-241. https://doi.org/10.1016/j.jma.2016.06.003
[21] N. Boshkov, *Surface and Coatings Technology* **172** (2003) 217-226. https://doi.org/10.1016/S0257-8972(03)00463-8
[22] D. S. Rodríguez, S. Kozhukharov, M. Machkova, V. Kozhukharov, *Bulgarian Chemical Communications* **45-A** (2013) 24-32. http://www.bcc.bas.bg/bcc_volumes/Volume_45_Special_A_2013/BCC-45-SE-A-24-32.pdf.
[23] S. Kozhukharov, J. A. P. Ayuso, D. S. Rodríguez, O. F. Acuña, M. Machkova, V. Kozhukharov, *Journal of Chemical Technology and Metallurgy* **48** (2013) 296-307. https://dl.uctm.edu/journal/node/j2013-3/11-Stefan_Kojukharov-296-307.pdf
[24] S. V. Kozhukharov, Ch. A. Girginov, *Classical and Modern Methods for Corrosion Impact Rate Determination for Aluminium and Strengthened Aircraft Alloys. Fundamentals and Practical Applications*, in *Phenomena and Theories in Corrosion Science. Methods of Prevention*, A. Gergely Ed., NOVA Sci. Publ., New York, USA, 2019, p. 3-150 ISBN 978-153-615253-1.
[25] S. Kozhukharov, Ch. Girginov, D. Kiradzhiyska, A. Tsanev, G. Avdeev, *Journal of Electrochemical Science and Engineering* **10** (2020) 317-334. https://doi.org/10.5599/jese.820
[26] M. Fairchild, *Color Appearance Models*, in *Color Appearance Models*, John Wiley and Sons, 2019, p. 199-212. https://doi.org/10.1002/9781118653128
[27] E. A. Matter, S. Kozhukharov, M. Machkova, V. Kozhukharov, *Journal of Chemical Technology and Metallurgy* **50** (2015) 52-64. https://dl.uctm.edu/journal/node/j2015-1/8_Stefan_Kojuharov_52-64.pdf
[28] K. Ignatova, S. Kozhukharov, G. Avdeev, I. Piroeva, *Bulgarian Chemical Communications* **50-A** (2018) 61-69. http://www.bcc.bas.bg/bcc_volumes/Volume_50_Special_A_2018/BCC-50-A-2018-61-69-Ignatova.pdf
[29] P. Atanasova, S. Kozhukharov, M. Milanes, *Annual Proceedings of the University of Rousse* **54** (2015) 42-46. http://conf.uni-ruse.bg/bg/docs/cp15/10.1/10.1-8.pdf
[30] F. Yu, W. F. Li, X. P. Chen, G. G. Zhang, *Materials Research Innovations* **19** (2015) S2-28-S2-34. https://doi.org/10.1179/1432891715Z.0000000001310

[31] A. Conde, M. A. Arenas, A. de Frutos, J. de Damborenea, *Electrochimica Acta* **53** (2008) 7760-7768. https://doi.org/10.1016/j.electacta.2008.05.039
[32] W. G. Fahrenholtz, M. J. O'Keefe, H. Zhou, J. T. Grant, *Surface and Coatings Technology* **155** (2002) 208-213. https://doi.org/10.1016/S0257-8972(02)00062-2
[33] D. K. Heller, W. G. Fahrenholtz, M. J. O'Keefe, *Corrosion Science* **52** (2010) 360-368. https://doi.org/10.1016/j.corsci.2009.09.023
[34] G. Tsaneva, V. Kozhukharov, S. Kozhukharov, M. Ivanova, J. Gerwann, M. Schem, T. Schmidt, *Journal of the University of Chemical Technology and Metallurgy* **43** (2008) 231-238. https://dl.uctm.edu/journal/node/j2008-2/9_Kojukharov_231.pdf
[35] S. V. Kozhukharov, *Advanced Multifunctional Corrosion Protective Coating Systems for Light-Weight Aircraft Alloys - Actual Trends and Challenges*, in *Thin Film Processes - Artifacts on Surface Phenomena and Technological Facets*, J. Thirumalai Ed., IntechOpen, 2017, p. 179-210. https://doi.org/10.5772/64990
[36] A. Pardo, S. Feliú Jr., M.C. Merino, R. Arrabal, E. Matykina, *Applied Surface Science* **254** (2007) 586-595. https://doi.org/10.1016/j.apsusc.2007.06.036
[37] E. Paparazzo, *Journal of Physics: Condensed Matter* **30** (2018) 343003. https://doi.org/10.1088/1361-648X/aad248
[38] C. Barth, C. Laffon, R. Olbrich, A. Ranguis, Ph. Parent, M. Reichling, *Scientific Reports* **6** (2016) 21165. https://doi.org/10.1038/srep21165
[39] F. Solís-Pomar, E. Martínez-Guerra, M. Meléndrez-Castro, E. G. Pérez-Tijerina, *Journal of Nano Research* **14** (2011) 145-154. https://doi.org/10.4028/www.scientific.net/jnanor.14.145
[40] S. J. An, J. Li, C. Daniel, D. L. Wood III, *Journal of The Electrochemical Society* **166** (2019) A1121-A1126. https://doi.org/10.1149/2.0591906jes
[41] R. Al-Gaashani, S. Radiman, A. R. Daud, N. Tabet, Y. Al-Douri, *Ceramics International* **39** (2013) 2283-2292. https://doi.org/10.1016/j.ceramint.2012.08.075
[42] H. Ma, Y. Tan, Z. Liu, J. Wei, R. Xiong, *New Journal of Chemistry* **45** (2021) 13860-13868. https://doi.org/10.1039/D1NJ00973G
[43] A. Furlan, J. Lu, L. Hultman, U. Jansson, M. Magnuson, *Journal of Physics: Condensed Matter* **26** (2014) 415501. https://doi.org/10.1088/0953-8984/26/41/415501
[44] V. Shutthanandan, M. Nandasiri, J. Zheng, M. H. Engelhard, W. Xu, S. Thevuthasan, V. Murugesan, *Journal of Electron Spectroscopy and Related Phenomena* **231** (2019) 2-10. https://doi.org/10.1016/j.elspec.2018.05.005
[45] X. Chen, X. Wang, D. Fang, *Fullerenes, Nanotubes and Carbon Nanostructures* **28** (2020) 1048-1058. https://doi.org/10.1080/1536383X.2020.1794851
[46] F. Brau, S. Thouvenel-Romans, O. Steinbock, S. Cardoso, J. Cartwright, *Soft Matter* **15** (2019) 803-812. https://doi.org/10.1039/C8SM01928B
[47] V. F. C. Lins, R. M. V. Paranhos, E. A. Alvarenga, *Journal of Materials Science* **42** (2007) 5094-5104. https://doi.org/10.1007/s10853-006-0554-1
[48] D. Spanoudaki, E. Pavlidou, D. Sazou, *ChemSystemsChem* **3** (2021) e2000054. https://doi.org/10.1002/syst.202000054
[49] K. Aramaki, *Corrosion Science* **43** (2001) 1573-1588. https://doi.org/10.1016/S0010-938X(00)00144-X
[50] F. H. Scholes, C. Soste, A. E. Hughes, S. G. Hardin, P. R. Curtis, *Applied Surface Science* **253** (2006) 1770-1780. https://doi.org/10.1016/j.apsusc.2006.03.010